Reduction of transverse emittance in electron injectors caused by space charge effects

A. Mizuno[a,*], K. Masuda[b], M. Yamamoto[c]

[a]*JASRI/SPring-8, 1-1-1 Koto, Sayo, Hyogo, 679-5198, Japan*
[b]*Institute of Advanced Energy, Kyoto University, Gokasho, Uji, Kyoto, 611-0011, Japan*
[c]*Accuthera Inc., 2-8-22, Kuriki, Aso, Kawasaki, Kanagawa, 215-0033, Japan*

Abstract

We report that transverse emittance can be reduced by the space charge effects in electron injectors. The reduction of emittance in an ideal DC-accelerated continuous beam is numerically calculated and the mechanisms of the reduction are analytically discussed. Beam edge and image charge effects at a cathode produce a particular nonlinearity in r-r' phase space, which is discussed in the paper, and they contribute to reducing the emittance immediately after the cathode. We also show examples of reduced emittance for practical electron injectors such as that in the SCSS thermionic gun with a continuous beam, and those in the SPring-8 rf photoinjector and the BNL-type rf photoinjector with pulsed beams. For pulsed beams, the focusing effects caused by an rf cavity also contribute to reducing the emittance. These reductions only appear when the beam charge is low.

Keywords: Emittance evolution, Electron injector, Space charge effects

1. Introduction

Research on emittance evolution is important for designing low-emittance electron injectors. For these injectors, the emittance compensation technique [1] is widely used. Using this technique, the transverse projected emittance of an

---

*Corresponding author
Email addresses: `mizuno@spring8.or.jp` (A. Mizuno), `masuda@iae.kyoto-u.ac.jp` (K. Masuda)

entire bunch can be reduced owing to the different rotation angle of each slice emittance in a phase space using beam-focusing devices. Details of the emittance variations in rf photoinjectors are described in Ref. [2]. This theory is valid even if each slice emittance in the bunch is constant.

For describing the beam dynamics in the electron injectors, the emittance is usually defined as an rms emittance. It can vary since the rms emittance is different from a constant volume of the Liouville's theorem. Therefore, investigation of evolution of the slice emittance is of the same importance as the emittance compensation technique described above.

There are many papers which describe the evolution of the slice emittance in electron injectors. In Refs. [3, 4, 5], they show simulation results calculated by MAFIA and Impact-T that the slice emittances of pulsed beams in rfgun cavities increase rapidly in the vicinity of the cathode, then they turn to decrease. In Ref. [6], the projected emittance of the bunch in the vicinity of a DC gun cathode is observed to decrease in the simulation by GPT. In Ref. [7], the emittances of DC continuous beam decrease immediately after a DC gun cathode in simulations calculated by KUAD2 and 3D FDTD.

In Refs. [3, 4], the authors pointed out that these increasings are caused by nonlinearity of space charge forces and subsequent decreasings are self-linearization of transverse phase space distribution caused also by nonlinearity of space charge forces, that is, the nonlinearity is compensated by the space charge force itself. The emittance decreasings in Ref. [6] are also thought to be due to the self-linearizations. These are not phenomena of emittance compensations caused by an electrode or the other extra forces but relaxation process of the space charge force itself, although detail mechanisms on self-linearization and eventual emittance reductions are not enough discussed.

Phenomena of decreasing or oscillating emittance are also reported in a high current induction linac [8, 9]. They are not caused by the self-linearization but by nonlinear fields of gun electrode or space charge fields produced by nonlinear charge distribution of the beam. These phenomena are also important for clearly understandings on emittance evolution.

The scope of this paper is to show analytical mechanisms for those self-linearizations and the emittance reductions. Making clear for these mechanisms could contribute to new approach for designing the low-emittance electron injectors.

In Sec. 2, we show the reduced emittance examples for an ideal DC-accelerated continuous beam which is caused by the same mechanism as described in Refs. [3, 4, 5, 6, 7]. In Sec. 3, we discuss the self-linearization mechanisms which cause emittance reductions analytically. In Sec. 4, we give further examples of reduced emittance for a practical DC gun with a continuous beam and practical rf photoinjectors with pulsed beams.

2. Emittance reduction in an ideal DC-accelerated continuous beam

We show an example of the calculated reduction of the transverse emittance for an ideal DC-accelerated continuous beam in Fig. 1. The initial conditions are given in Table 1.
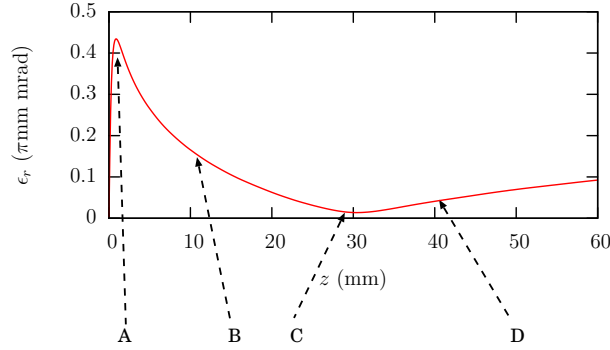

Figure 1: Emittance behavior along a beam axis for an ideal DC-accelerated continuous beam. Points A, B, C and D are used for discussions in Sec. 3.

A continuous beam with an initial thermal emittance of 0 mrad is extracted from a perfectly conducting planar cathode at $z = 0$ m. The calculation takes into account the image charge effects at the cathode. After the beam is extracted, it is continuously accelerated by a uniform DC electric field, E_z.

3

Table 1: Parameters for an ideal DC-accelerated continuous beam.

Extracted current from cathode	40 A/cm^2
Initial beam spot size	ϕ 2.0 mm uniform
Applied electric field, E_z	5.0 MV/m
Accelerated region	in all of a calculation area

The calculation is performed using the two-dimensional code KUAD2 [10], which solves the Maxwell equations by the finite element method using fine quadratic triangular elements in a calculation area. Electron trajectories are traced from one boundary ($z = 0$ m) to the other ($z = 100$ mm) in the calculation area. The traces are iterated until the trajectories converge. Therefore, this code is only suitable for a continuous beam, and the space charge effects including the image charge effects at the cathode are expected to be calculated accurately.

The normalized transverse emittance is defined as

$$\epsilon_r\left(z\right) = \sqrt{\langle r^2\rangle_z \left\langle\left(\gamma\beta r'\right)^2\right\rangle_z - \langle\gamma\beta r r'\rangle_z^2}, \tag{1}$$

where β is the particle velocity normalized by the light velocity in vacuum, γ is the Lorenz factor of the particles, and the brackets $\langle\rangle_z$ denote the average of each traced particle parameter when the particle passes point z. This definition of emittance is comparable to that of the slice emittance rather than to that of the projected emittance of a bunch. The emittance increases rapidly immediately after the cathode, then decreases and starts to increase again at $z = 30$ mm.

Figure 2 shows the emittance reductions calculated by KUAD2 and GPT[11], which is a more widely used code than KUAD2. In GPT, the spacecharge2Dcircle element is used in the space charge calculation. Using this element, each particle is represented as a symmetrical circle about the beam axis, whose radius is equal to that of the particle itself. The space charge fields are calculated as sum of fields produced by each circle, and tracking of each particle is performed with these space charge fields. The other elements in GPT could not reproduce
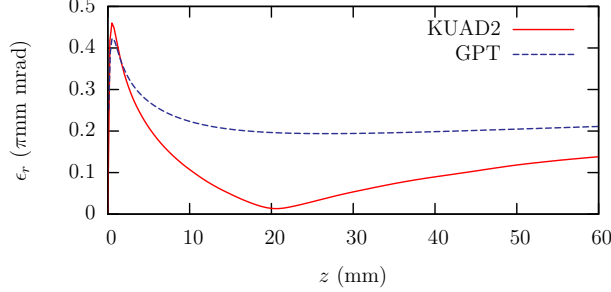
4

Figure 2: Emittance reductions calculated by KUAD2 and GPT. The image charge effects at the cathode are not taken into account.

the reduction phenomena. The spacecharge2Dcircle element cannot model the image charge effects at the cathode, therefore they are not taken into account in the calculation by KUAD2 for comparison in Fig. 2. Minimum emittance values are not in agreement between the two codes, although significant features in the emittance reduction are observed in both cases.

Figure 3(a) shows the minimum emittance as a function of the number of particles used in GPT. The number of particles used in the calculation in Fig. 2 is 2×10^4, which corresponds to the leftmost plot in Fig. 3(a). The emittance still does not converge. Increasing the number of particles in GPT may result in more significant emittance reduction, although we cannot show the calculation results because of the calculation time. Meanwhile, the number of trajectories used in the calculation by KUAD2 in Fig. 1 is 4096, which corresponds to the leftmost plot in Fig. 3(b). In this case, the emittance converges satisfactorily. The number of trajectories used in the calculation by KUAD2 in Fig. 2 is also 4096. Therefore, the calculation by KUAD2, which shows good convergence, is expected to be more accurate than that by GPT with a limited number of particles. This is entirely because GPT is a time domain code and accordingly requires a longer calculation time than KUAD2, which is specially designed only for the simulations of continuous beams.

These evolution patterns of emittance are similar to the phenomena described in Ref. [3, 4, 5, 6, 7].

5
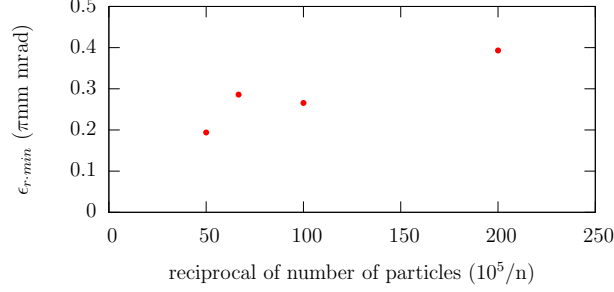
(a) Dependence of minimum emittance on number of particles used in GPT for the calculation shown in Fig. 2.
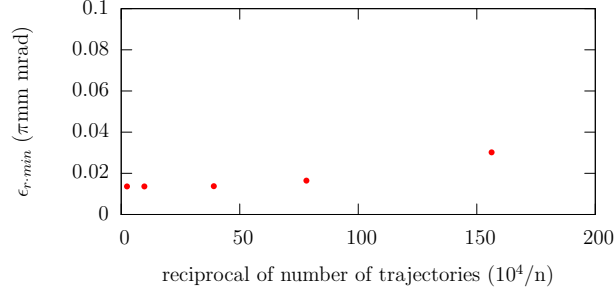
(b) Dependence of minimum emittance on number of trajectories used in KUAD2 for the calculation shown in Fig. 1. Image charge effects at the cathode are taken into account.

Figure 3: Minimum emittances calculated by GPT and KUAD2.

3. Mechanisms of emittance reduction

3.1. Invariance of transverse emittance

The transverse rms emittance remains constant when transverse linear forces act on each particle. Here, we consider r emittance instead of x or y emittance to simplify the subsequent discussion.

As shown in Fig. 4, two arbitrary particles among the particles lying on the gray line in the figure are at position vectors $\mathbf{a}$ and $\mathbf{b}$ in the r-r' phase space at time t, and they move to positions $\mathbf{a}$' and $\mathbf{b}$', respectively. The area of the parallelogram formed by vectors $\mathbf{a}$ and $\mathbf{b}$ is defined as W. Increases and decreases in W correspond to those in the transverse emittance. Note that both
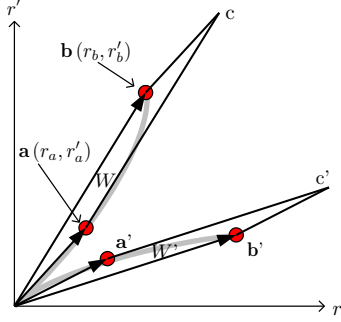
6

Figure 4: Concept of emittance invariance.

W in Fig. 4 and the r emittance in Eq. (1) are defined with respect to the origin $r = r' = 0$, which is always the center of the ensemble of the particles because cylindrical symmetry is assumed. W is expressed as

$$W = \vec{\mathbf{a}} \times \vec{\mathbf{b}} = r_a r_b' - r_a' r_b. \tag{2}$$

The derivative of W is

$$\frac{dW\,(t)}{ds} = r_a r_b'' - r_a'' r_b. \tag{3}$$

If $r'' = Kr$, which corresponds to the condition that only linear forces act on the particles, Eq. (3) becomes zero. Therefore, the transverse emittance is constant.

3.2. Increases and decreases in transverse emittance

If $r'' \neq Kr$, the transverse emittance does not remain constant. In the subsequent discussion, it is convenient that W is defined as positive. Under this condition, the emittance increases when $dW/ds > 0$ and decreases when $dW/ds < 0$. Therefore, θ_a, which is the angle between vector $\mathbf{a}$ and the r-axis in the phase space, must be chosen to be smaller than θ_b since W is defined by Eq. (2).

First, the r-r' phase space is shown in Fig. 5 in the case that $r_a > r_b$. We consider an ideal beam that is symmetrical about the beam axis and whose
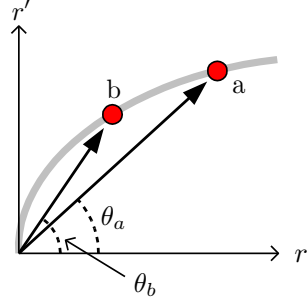
7

Figure 5: Phase space illustration for $r_a > r_b$.

initial thermal emittance is 0 mrad. The particle plots in the r-r' phase space shown in gray in Fig. 5 form a single line because of the symmetry and the absence of thermal emittance. Moreover, a convex upward curve is formed since $\theta_a < \theta_b$. Under this condition, we assume that K is not constant and we define $r'' \equiv K(r) r$. Then this gray line in the phase space is generated by particles on which forces whose transverse distributions satisfy $dK(r)/dr < 0$ have acted. This shape in the phase space is often observed when a beam propagates with electrons in the beam diffusing transversely as a result of space charge forces.

Here, we discuss the situation that nonzero forces act on particles a and b in Fig. 5. We define these forces for particles a and b as follows:

$$
\begin{cases}
r_a'' & \equiv K_a r_a \\
r_b'' & \equiv K_b r_b.
\end{cases}
\tag{4}
$$

Then in this case, dW/ds is expressed as

$$
\frac{dW}{ds} = (K_b - K_a) r_a r_b.
\tag{5}
$$

Therefore, if $K_b > K_a$, the emittance increases. In this case, forces whose transverse distributions satisfy $dK(r)/dr < 0$ continuously act on the particles since $r_a > r_b$, and this is the usual case.

In contrast, if $K_b < K_a$, the emittance decreases. Forces whose transverse distributions satisfy $dK(r)/dr > 0$ act on the particles. This case is considered

8

not to occur for space charge effects in continuous beams in free space.
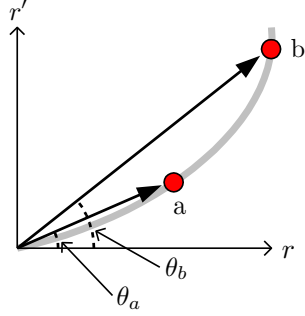

Figure 6: Phase space illustration for $r_a < r_b$.

In the case that $r_a < r_b$, the r-r' phase space is shown in Fig. 6. Particle plots in the phase space form a gray line that is convex downward. This line is generated by particles on which space charge forces whose transverse distributions satisfy $dK(r)/dr > 0$ have acted. This shape in the phase space often appears immediately after a perfectly conducting cathode, even if the initial radial current distribution is uniform as in the case shown in Fig. 1.

We consider a cylindrical electron beam emitted from a planar cathode schematically shown in Fig. 7. The equipotential line lies on the cathode surface owing to the image charge effects. However, the line becomes warped at a short distance from the cathode. Therefore, the radial components of the space charge forces on the outer side of the beam are enhanced and the phase space shape shown in Fig. 6 is realized.

Even if the image charge effects at the cathode are not taken into account in the calculation, as shown in Fig. 2, a convex downward shape is still formed immediately after the cathode.

In the case of continuous beams or high-energy pulsed beams with uniform density, the beam produces radially linear space charge forces. We consider the beam as a combination of an inner solid cylinder and a surrounding hollow circular cylinder, with an electron A located between the two parts. The space charge force generated by the inner part of the beam acts on electron A but the
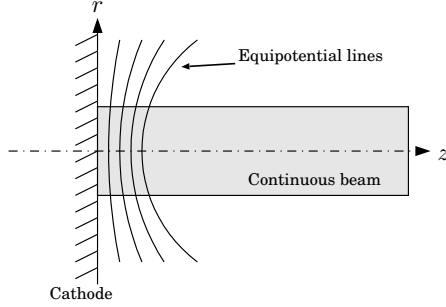
9

Figure 7: Schematic illustration of equipotential lines near the cathode.

force generated by the surrounding part does not act on electron A. Therefore, the force generated by the space charge becomes radially linear.

However, in the case of beam generation at the cathode discussed here, electron A is focused by the surrounding part of the beam owing to the existence of a beam edge at the cathode. This force on electron A partially cancels the defocusing force applied by the inner part of the beam. The amount of cancellation is greater on the inner side of the beam. Therefore, the nonlinearity of the space charge forces appears, which is the other cause of the convex downward phase space plot immediately after the cathode.

As an example, Fig. 8(a) shows the plot in the r-r' phase space at $z = 0.1$ mm for the calculation by KUAD2 in which the image charge effects at the cathode are taken into account and whose results are shown in Fig. 1. The line in the phase space is convex downward. Fig. 8(b) shows the r-r' phase space plots for the calculations by GPT and KUAD2 in which the image charge effects are not taken into account and whose results are shown in Fig. 2. The shape of the plots is also convex downward.

Figure 9 shows radial current density distributions and r-r' phase space plots immediately after the cathode and at points A, B, C and D for the calculation shown in Fig. 1. The current density distribution is radially uniform immediately after the cathode ($z = 0.1$ mm) and the phase space shape is convex downward. After that, the current density on the outer side of the beam de-

10
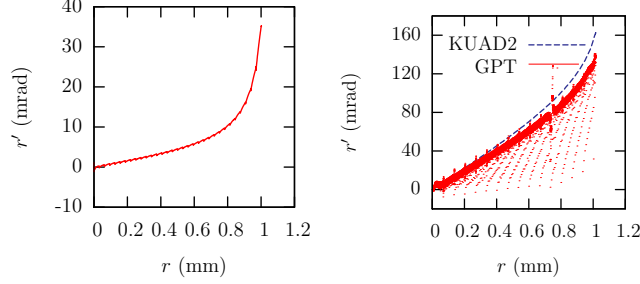
(a) For the calculation shown in Fig. 1.

(b) For the calculations shown in Fig. 2.

Figure 8: Phase space plots at $z = 0.1$ mm for the calculations shown in Figs. 1 and 2.

creases rapidly at point A, where the emittance becomes maximum. This is due to the space charge forces originating from the beam edge, which include the image charge effects with transverse distributions satisfying $dK(r)/dr > 0$. These forces correspond to the case of $K_b > K_a$ since the phase space shape is convex downward. They continue to act on the particles from the cathode to point A. The emittance also increases when $K_b > K_a$ and decreases when $K_b < K_a$ in the same manner as in the case of $r_a > r_b$. Therefore, the transverse emittance shown in Fig. 1 increases from the cathode to point A.

After point A, the contributions of the beam edge and the image charge effects to the space charge effects are decreased and the current density distribution becomes a downward-sloping curve from the beam center. In this case, forces with transverse distributions satisfying $dK(r)/dr < 0$ act on the particles due to beam propagation with particles diffusing transversely as mentioned before. On the other hand, the shape of the r-r' phase space remains convex downward. Therefore, these forces correspond to the case of $K_b < K_a$. As a result, the emittance starts to decrease at point A as shown in Fig. 1.

At point B, as shown in Fig. 9(b), $dK(r)/dr$ in the phase space plot decreases owing to space charge effects which is called self-linearizing process in Ref. [4]. At point C, the phase space plot forms a straight line, that is, the space charge force is almost completely self-linearized. Therefore, the emittance

11
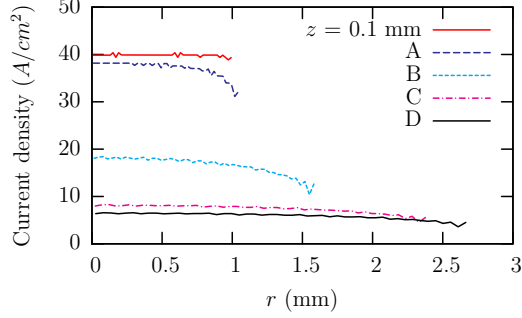
(a) Radial current density distributions.
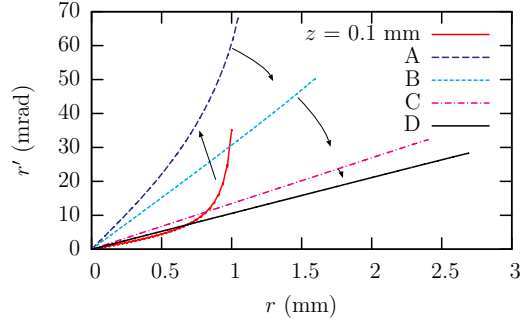
(b) r-r' phase space plots.

Figure 9: Radial current density distributions and r-r' phase space plots immediately after the cathode and at points A, B, C and D for the calculation shown in Fig. 1.

becomes minimum value.

After point C, $dK\left(r\right)/dr$ becomes negative, that is, the shape of the phase space becomes convex upward at point D. On the other hand, the forces with transverse distributions satisfying $dK\left(r\right)/dr < 0$ continue to act on the parti-
cles, corresponding to the case that $K_b > K_a$. Therefore, the emittance starts to increase; nevertheless, the phase space plots at B, C and D in Fig. 9(b) are only slightly curved and we cannot distinguish whether the plots are convex upward or downward.

In Fig. 10, the second derivatives of the line in the phase space at B and D are plotted as a function of r. d^2r'/dr^2 is positive at B, therefore we can clearly recognize that the shape of the phase space at B is convex downward, whereas
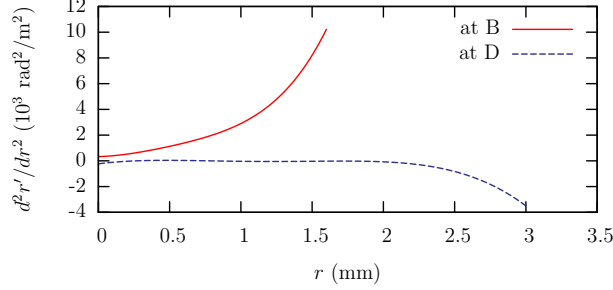
12

Figure 10: Second derivatives of the line in the phase space at B and D plotted as a function of r.

it is convex upward at D since d^2r'/dr^2 is negative.

Since these emittance reductions are caused by the space charge effects, reduction patterns vary with conditions of the extracted beams. Figure 11 shows emittance behaviors along a beam axis for the same situations of Fig. 1, with various applied electric fields and extraction current densities calculated by KUAD2. The image charge effects at the cathode are taken into account. In Fig. 11(a), emittance reduction due to the self-linearization is more significant with a lower applied electric field, because the space charge forces take an important role in the self-linearization process which is discussed above. Importantly, one can see in the Fig. 11(a) that the lowest applied electric field among the three may result in the lowest emittance, at $z = 30$ mm for example. Also important to note is that, in Fig. 11(b), the distance from the cathode to the point where emittance takes a minimum depends strongly on the initial parameters, implying possible gun design and/or choice of operating parameters to minimize emittance at a successive accelerating structure. These results suggest importance of understanding the self-linearization in a practical injector design.

Note that if we discuss these mechanisms using x or y emittance instead of r emittance, the single lines in Figs. 5 and 6 both become two-dimensional to form the area shown in Fig. 12. Moreover, they cannot be distinguished from each other. Therefore, we use r emittance for our discussion, which can be easily

13
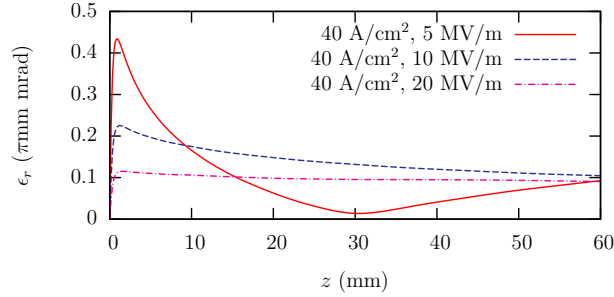
(a) Comparison among three different applied fields for a fixed extraction current density.
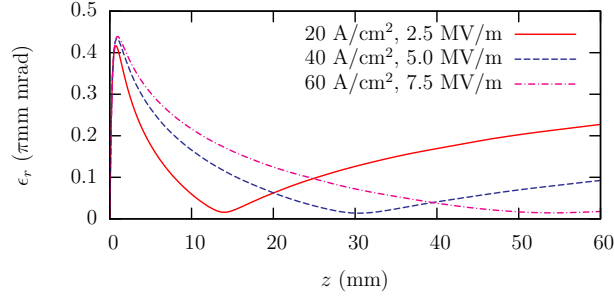
(b) Comparison among three different sets of applied field and extraction current density with a fixed field - current ratio.

Figure 11: Emittance behaviors along a beam axis for an ideal DC-accelerated continuous beam calculated by KUAD2 with various initial parameters. The image charge effects at the cathode are taken into account.

changed to x or y emittance if there is no coupling between x and y. Also, if we consider the initial thermal emittance, even the r-r' phase space plot has an area. Therefore, the initial thermal emittance cannot be reduced by these mechanisms.

4. Reduction of emittance in practical injectors

Here, we show examples of reduced emittance in practical injectors. One is in a thermionic gun with a continuous beam and the others are in rf photoinjectors with pulsed beams.
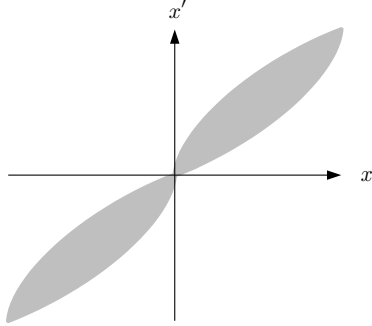
14

Figure 12: Plot in x-x' phase space corresponding to the single lines in the r-r' phase space shown in Figs. 5 and 6.

4.1. Reduction of emittance in the SCSS thermionic gun

The emittance behavior in the SCSS thermionic gun [12] calculated by KUAD2 is shown in Fig. 13. The parameters used in the calculation are listed in Table 2. The pulse length of the beam is 3.0 μs in practice. In the calculation, however, we assume a DC continuous beam since the aspect ratio of the pulse length to the beam radius is sufficiently large. A perfectly conducting cathode is located at $z = 0$ m, and a continuous beam is extracted from the cathode by a DC electric field, which is applied between the cathode and an anode. The image charge effects at the cathode are taken into account. After reaching the anode, which is located at $z = 50$ mm, the beam propagates in free space to $z = 0.9$ m. Although there is a small bump at the anode, a reduction of emittance is clearly observed, and a point of minimum emittance also appears at point C.

Table 2: Parameters used in calculation for the SCSS thermionic gun.

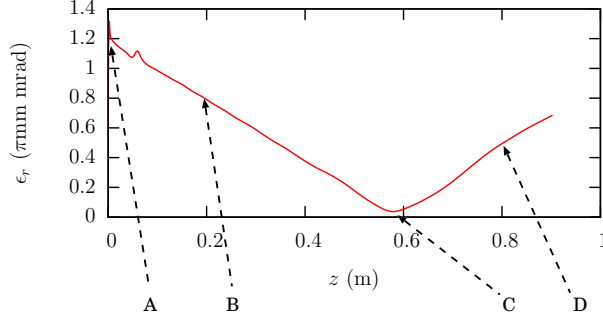|	
Extracted current from cathode	1.0 A
Initial beam spot size	ϕ 3.0 mm uniform
Voltage applied between cathode and anode	500.0 kV
Initial thermal emittance	0 mrad

Figure 13: Reduction of emittance in the SCSS thermionic gun.

Figure 14 shows radial current density distributions and r-r' phase space plots at points A ($z = 1.4$ mm), B, C and D for the calculation shown in Fig. 13. Since the scales of the graphs of the current density distribution at A and at B−D are extremely different, the figures for A and B−D are shown separately. The evolutions of the current density distributions and the shape of the phase space have the same features as those shown in Fig. 9; therefore, the emittance reduction in the calculation shown in Fig. 13 occurs via the same mechanism as that discussed in Sec. 3.

In Ref. [12], the normalized x emittance at $z = 0.5$ m measured by the double-slit method is reported. It was 0.6 π mm mrad at 90% core emittance including an initial thermal emittance of 0.4 π mm mrad. Therefore, the x emittance without including the thermal emittance becomes 0.45 π mm mrad, which corresponds to 0.9 π mm mrad in terms of the r emittance, since the r emittance is twice of the x emittance in the case of an axisymmetrical beam. In contrast, as shown in Fig. 13, the calculated r emittance at $z = 0.5$ m, which does not include the initial thermal emittance, is 0.2 π mm mrad and lower than the measured value. The emittance without including the thermal emittance is extremely low and comparable to the thermal emittance, making it difficult to measure accurately. Emittance measurements at various points are necessary for comparison with simulation results.

16
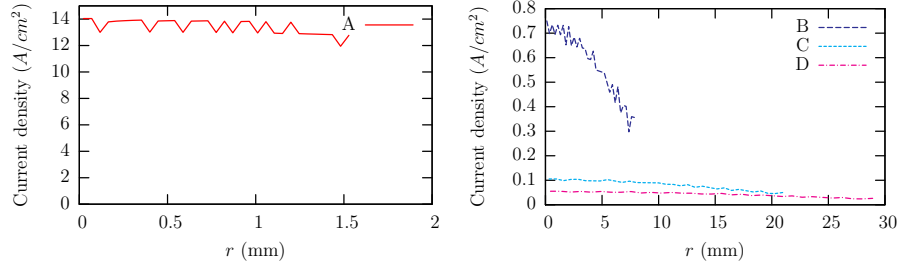
(a) Radial current density distribution at point A.

(b) Radial current density distributions at points B−D.
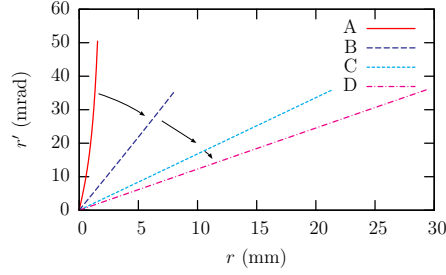
(c) r-r' phase space plots.

Figure 14: Radial current density distributions and r-r' phase space plots at points A, B, C and D for the calculation shown in Fig. 13.

4.2. Reduction of emittance in the SPring-8 rf photoinjector

²⁷⁵ In the next two sections, we discuss the reduction of emittance in rf photoinjectors with pulsed beams. Therefore, the emittance is not a slice emittance but a projected emittance of an entire bunch, and is defined as

$$\epsilon_r\left(\langle z\rangle_t\right) = \langle\gamma\rangle_t\,\langle\beta\rangle_t\,\sqrt{\langle r^2\rangle_t\,\langle r'^2\rangle_t - \langle r\cdot r'\rangle_t^2}, \tag{6}$$

where the brackets $\langle\rangle_t$ denote the average of each parameter for the entire bunch at time t. γ and β are placed outside of the root since the emittance based on ²⁸⁰ this definition can be measured practically.

Figure 15 shows time evolutions of the emittance for the SPring-8 rf photoinjector. The emittances shown in Fig. 15(a) are calculated using the two-dimensional multiple beam envelope equations [13] because of their high accu-

17

racy for calculating the projected emittance of a pulsed beam. Fig. 15(b) shows

the emittances calculated by GPT for comparison. The spacecharge3Dmesh
element is used in the space charge calculation in GPT. A perfectly conducting
cathode is located at $z = 0$ m and a single-cell S-band rf gun cavity [14] is
located from $z = 0$ to 75 mm. The beam propagates in free space to $z = 1.6$ m
after reaching the cavity exit. The image charge effects at the cathode are taken
into account in both calculations. The parameters used in the calculations are
shown in Table 3, which are normal operation parameters.
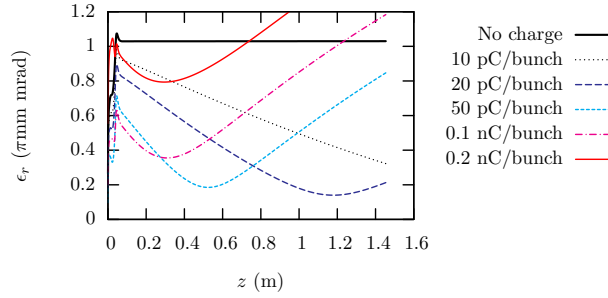
(a) Calculated using multiple beam envelope equations.
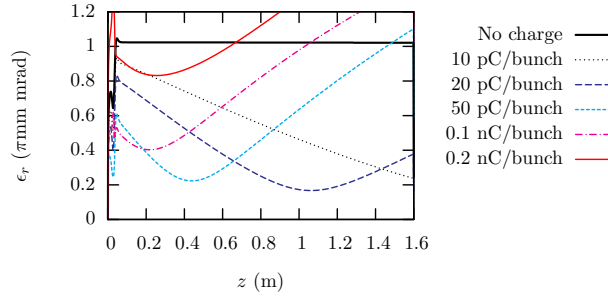
(b) Calculated by GPT.

Figure 15: Reductions of emittance in the SPring-8 rf photoinjector.

The black straight solid lines in Figs. 15(a) and 15(b) show the results with-
out calculating the space charge effects, for which the emittance remains con-
stant after the cavity. These emittances correspond to rf emittances. The other
lines are calculated taking account of the space charge effects. The emittances
decrease after the cavity exit and become smaller than the rf emittances. There-

Table 3: Parameters used in calculations for the SPring-8 rf photoinjector.

Laser width	20 ps uniform
Laser spot size	ϕ 1.2 mm uniform
Laser spot size for Fig. 17	ϕ 0.9 mm - ϕ1.4 mm
Maximum electric field on cathode surface	157.0 MV/m
Beam energy at exit of cavity	3.6 MeV
Initial rf phase	sin 5 deg.
Initial emittance	0 mrad

fore, these reductions of emittance are caused by the space charge effects. After that, minimum emittances appear, then the emittances start to increase. The emittance behaviors are in agreement for the two calculations.

Figure 16 shows time evolutions of the slice emittance for the calculation shown in Fig. 15(a) whose charge per bunch is 50 pC. Note that Fig. 16 and the subsequent results are calculated using the multiple beam envelope equations. In Fig. 16(a), the time evolutions close to the cathode are shown. The longitudinal electric field along the axis of the cavity is also plotted to indicate the position of the cavity. Each slice emittance decreases in the cavity. However, the projected emittance varies in the cavity and its behavior is uncorrelated to that of the slice emittance. In the rf cavity, the energy of each slice becomes different and the radial force caused by the rf field has a time dependence. Therefore, the variation of the projected emittance in this region is caused by the different amounts of rotation of each slice in the phase space.

In contrast, after the cavity, as shown in Fig. 16(b), each slice emittance continues to decrease, and the projected emittance also decreases (see Fig. 15). The position of the minimum projected emittance almost corresponds to those of each slice emittance. Therefore, the reduction of the projected emittance is mainly dominated by those of each slice emittance itself after the cavity.

In Fig. 17, the reciprocal of the distance from the cavity exit to the position of

19
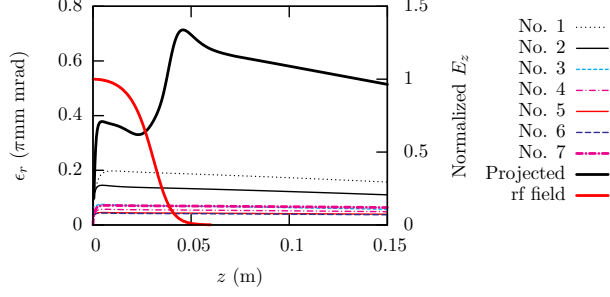
(a) Reductions in the rf gun cavity.
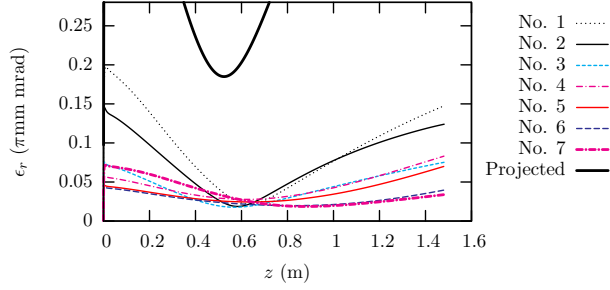
(b) Reductions in and after the rf gun cavity.

Figure 16: Reductions of slice emittance in the SPring-8 rf photoinjector in the case of 50 pC/bunch. Slice No.1 corresponds to the head of the bunch and slice No.7 corresponds to the tail. The projected emittance is also plotted for comparison.

minimum emittance is plotted as a function of initial charge density for various initial laser spot sizes. When the initial charge density is less than 20 pC/mm^2, the reciprocal of the distance is almost proportional to the charge density. These features are useful for optimum designing of the injectors for successive focusing devices and accelerating structures as is the case in the DC continuous beams.

When the initial charge density is larger than 20 pC/mm^2, it is not proportional because the large nonlinear space charge forces break up the convex downward shape in the phase space. In Fig. 15, reductions of the emittance are not clearly observed when the charge is more than 0.2 nC/bunch for the same reason.

Figure 18 shows the result of a simulation for the SPring-8 rf photoinjector, along with the result obtained when the image charge effects at the cathode
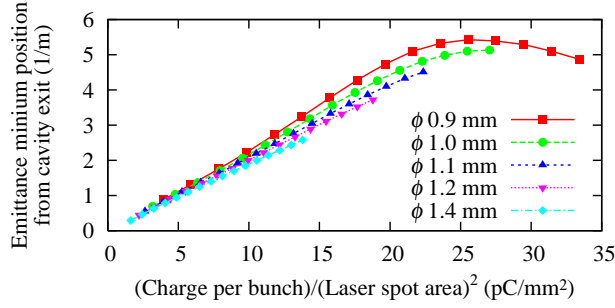
20

Figure 17: Reciprocal of distance from the cavity exit to position of minimum emittance as a function of initial charge density. The initial laser spot size is varied from ϕ 0.9 mm to ϕ 1.4 mm.

are not taken into account. The charge per bunch is 50 pC. Even when the image charge effects are not taken into account, the emittance is reduced as in the case of DC continuous beams. The emittance decreasing ratio obtained when calculating the image charge effects is slightly greater than that without calculating the image charge effects.

Phase space plots for each slice of the entire bunch immediately after the cathode for both cases are shown in Fig. 19. Each line corresponds to one slice of the bunch. The lowest line corresponds to the head of the bunch and the top line corresponds to the tail. Each plotted line is convex downward in both cases, and these shapes cause the emittance reductions.
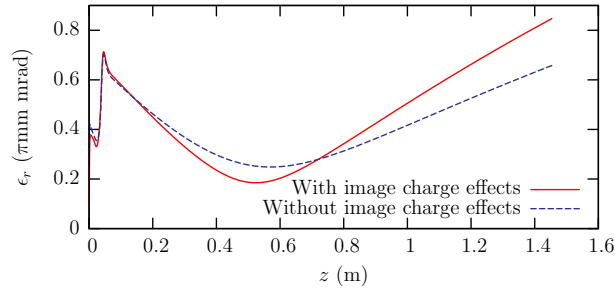

Figure 18: Reductions of emittance in the SPring-8 rf photoinjector with and without calculating the image charge effects at the cathode. The charge per bunch for both calculations is 50 pC.

21

(a) Calculations with image charge effects.

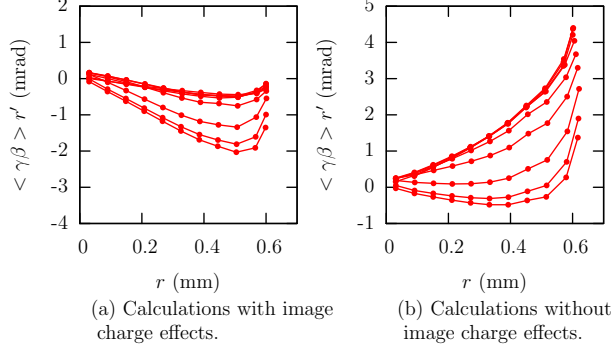(b) Calculations without image charge effects.

Figure 19: Phase space plots immediately after the cathode, $z = 0.5$ mm, with and without calculating the image charge effects. The lowest line corresponds to the head of the bunch and the top line corresponds to the tail. The charge per bunch for both calculations is 50 pC.

Figure 20 shows time evolutions of the transverse beam radius in the SPring-8 single-cell rf gun cavity near the cathode. A focusing force acts on the beam, which is generated by the image charge effects at the cathode. Therefore, the beam is defocused at the cathode in the case that the image charge effects are not considered in the calculation. After exiting the cathode, the beams are strongly focused by electromagnetic fields of the rf cavities in both cases. These rf fields, B_θ, are set to be proportional to the transverse position r in the calculation since the beam radius is sufficiently small. However, these focusing forces due to the rf fields and image charge effects compress the convex downward shape and enhance the nonlinearity in the phase space. Therefore, the emittance decreasing ratio becomes slightly larger when the image charge effects are taken into account.

These nonlinearities in the space charge forces satisfying $dK\left(r\right)/dr > 0$ near the cathode change to those satisfying $dK\left(r\right)/dr < 0$ as the beam propagates, since the nonlinearity disappears and electrons in the bunch diffuse transversely, that is, the space charge forces are self-linearized at higher energies. Therefore, the emittance is subsequently reduced.
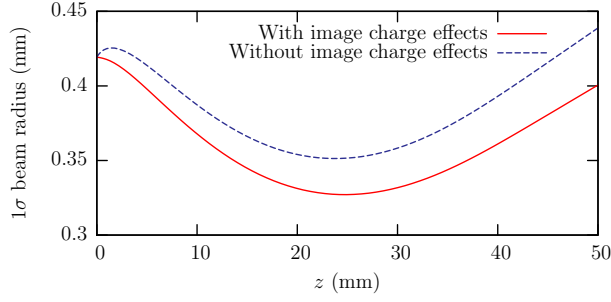
22

Figure 20: Time evolutions of transverse beam radius in the SPring-8 single-cell rf gun cavity with and without calculating the image charge effects at the cathode. The charge per bunch for both calculations is 50 pC.

4.3. Reduction of emittance in the BNL-type rf photoinjector

Figure 21 shows time evolutions of emittance for an rf photoinjector using the 1.6 cell BNL-type rf gun cavity. The cavity structure is located from $z = 0$ to 77.67 mm. The parameters used in the calculations are listed in Table 4, which are from Ref. [15]. The image charge effects at a perfectly conducting cathode are taken into account. They are also calculated using the multiple beam envelope equations. The emittances are also reduced in the BNL-type rf photoinjector, although the reduction is less than that in the SPring-8 rf photoinjector.
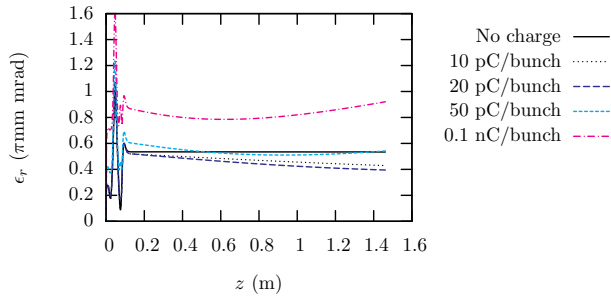

Figure 21: Reductions of emittance in the BNL-type rf photoinjector.

Figure 22 shows the beam energy at the exit of the BNL-type cavity as a function of the initial rf phase along with that for the SPring-8 cavity. The

23

Table 4: Parameters used in the calculations for the BNL-type rf photoinjector.

Laser width	10 ps uniform
Laser spot size	ϕ 1.3 mm uniform
Maximum electric field on cathode	120.8 MV/m
Energy at exit of cavity	5.75 MeV
Initial rf phase	sin 25 deg.
Initial emittance	0 mrad

initial rf phase ϕ_0 is defined as

$$E_z\left(t\right) = E_0 \sin\left(\omega t + \phi_o\right), \tag{7}$$

where $E_z\left(t\right)$ is the longitudinal electric field in the cavity. The head of the bunch is emitted when $t = 0$. The optimum initial rf phase for the BNL-type cavity is approximately 25 deg since the energy is maximized and the energy spread of the bunch is minimized at this phase. However, for the SPring-8 cavity, the optimum phase is 5 deg. Therefore, in the BNL-type cavity, the focusing force at the cathode generated by the rf field is weaker than that in the SPring-8 cavity, and the reduction of emittance is considered to be smaller.
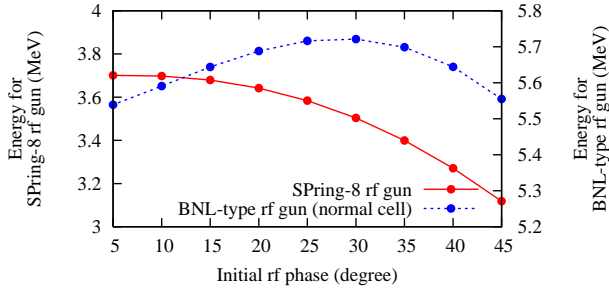

Figure 22: Bunch energy at the exit of the gun cavity as a function of initial rf phase.

The optimum phase depends on the longitudinal length of the first cell of the gun cavity. The lengths are 28 mm for the SPring-8 cavity and 23.1 mm for the BNL-type cavity in the calculations whose results are shown in Fig. 22.

24

If the length of the latter is increased to 28 mm, the optimum phase for the modified BNL-type cavity becomes the same as that for the SPring-8 cavity as shown in Fig. 23.
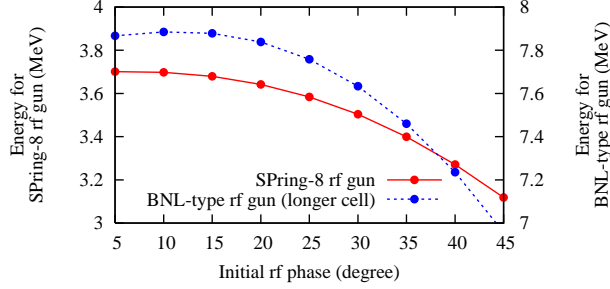

Figure 23: Bunch energy at the exit of the gun cavity as a function of initial rf phase. The length of the first cell of the BNL-type cavity is increased to 28 mm.

The time evolutions of emittance for the modified BNL-type rf photoinjector with the 28 mm cell cavity are shown in Fig. 24. The parameters used in the calculations are listed in Table 5. The laser width, the maximum electric field at the cathode, and the initial rf phase are set to be the same as those for the SPring-8 rf photoinjector. Therefore, the focusing effects caused by the rf field are almost equal for both cavities. The energy of the beam at the exit of the modified BNL-type cavity is different from that of the SPring-8 cavity. Therefore, the reductions of emittance are not the same. However, the reduction of emittance for the longer cell cavity is greater than that for the BNL-type rf photoinjector with the normal cavity, as shown in Fig. 21.

5. Conclusion

We investigated the reduction of transverse emittance in electron injectors immediately after the cathode caused by the self-linearizations of space charge forces. Plots in r-r' phase space become a convex downward single line immediately after the cathode. This line shape is formed by the image charge forces at the cathode and also nonlinear forces formed by the beam edge at the cathode, whose transverse distributions satisfy $dK(r)/dr > 0$. The emittance is reduced
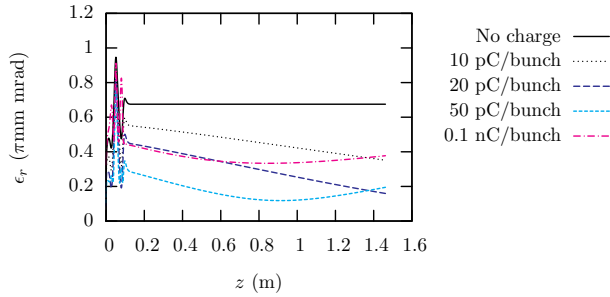
25

Figure 24: Reductions of emittance in the modified BNL-type rf photoinjector. The length of the first cell of the cavity is increased to 28 mm.

Table 5: Parameters used in the calculations for the modified BNL-type rf photoinjector. The length of the first cell of the cavity is increased to 28 mm.

Laser width	20 ps uniform
Laser spot size	ϕ 1.0 mm uniform
Maximum electric field on cathode	157.0 MV/m
Energy at exit of cavity	7.87 MeV
Initial rf phase	sin 5 deg.
Initial emittance	0 mrad

when space charge forces with distributions satisfying $dK(r)/dr < 0$ act on the beam after exiting the cathode.

⁴⁰⁰ We show examples of the reductions of the emittance for practical injectors, such as that in the SCSS thermionic gun as an example of a continuous beam, and those in the SPring-8 rf photoinjector and the BNL-type rf photoinjector as examples of pulsed beams.

For pulsed beams, the convex downward shape in the phase space immedi-
⁴⁰⁵ ately after the cathode is enhanced by the focusing force of the rf cavity field. Reductions of emittance are observed in both the SPring-8 rf photoinjector and the BNL-type rf photoinjector, although the reduction in the BNL-type rf photoinjector is significantly less than that in the SPring-8 photoinjector, since the rf focusing force is weaker in the BNL-type cavity.

26

In the SPring-8 rf photoinjector, a significant reduction of emittance is observed. However, it is not clearly observed for a charge exceeding 0.2 nC/bunch because large nonlinear space charge forces break up the convex downward shape in the phase space. Therefore, these phenomena will be useful for low-charge applications.

Acknowledgments

References

[1] B. E. Carlsten, Nucl. Instrum. Methods Phys. Res., Sect. A **285**, 313 (1989).

[2] L. Serafini and J. B. Rosenzweig, Phys. Rev. E **55**, 7565 (1997).

[3] R. Cee, M. Krassilnikov, S. Setzer, T. Weiland and A. Novokhatski, Nucl. Instrum. Methods Phys. Res., Sect. A **483**, 321 (2002).

[4] Zhirong Huang, Yuantao Ding and Ji Qiang, Nucl. Instrum. Methods Phys. Res., Sect. A **593**, 148 (2008).

[5] M. Krassilnikov, S. Setzer, T. Weiland and A. Novokhatski, in *Proceedings of the 2001 Particle Accelerator Conference, Chicago, USA* (2001), p.2257.

[6] Ivan V. Bazarov, Bruce M. Dunham, Colwyn Gulliford, Yulin Li, Xianghong Liu, Charles K. Sinclair, and Ken Soong, Phys. Rev. ST Accel. Beams **11**, 100703 (2008).

[7] K. Kasamsook, K. Nanbu, M. Kawai ,K. Akiyama, F. Hinode, T. Muto , T. Tanaka, M. Yasuda and H. Hama, in *Proceedings of FEL 2006,Berlin,Germany* (2006), p.680.

[8] B. E. Carlsten, Phys. Plasmas **6**, 3615 (1999).

[9] B. E. Carlsten, Phys. Rev. E **60**, 2280 (1999).

[10] K. Masuda, PhD thesis, Kyoto University (1997). Available online: http://hdl.handle.net/2433/24255

[11] Pulsar Physics, http://www.pulsar.nl/gpt

[12] K. Togawa, T. Shintake, T. Inagaki, K. Onoe and T. Tanaka, Phys. Rev. ST Accel. Beams **10**, 020703 (2007).

[13] A. Mizuno, H. Dewa, T. Taniuchi, H. Tomizawa, H. Hanaki and E. Hotta, Phys. Rev. ST Accel. Beams **15**, 064201 (2012).

[14] T. Taniuchi, T. Asaka, H. Dewa, T. Kobayashi, A. Mizuno, S. Suzuki, H. Tomizawa, K. Yanagida and H. Hanaki, in *Proceedings of the 21th International Linac Conference, Gyeongju, Korea* (2002), p.683.

[15] R. Akre *et al.*, Phys. Rev. ST Accel. Beams **11**, 030703 (2008).